



# Bombardment of Lunar Polar Crater Interiors by Out-of-ecliptic Ions: ARTEMIS Observations

Q. Nénon<sup>1,2</sup>  and A. R. Poppe<sup>1,2</sup> <sup>1</sup> Space Sciences Laboratory, University of California at Berkeley, Berkeley, CA USA<sup>2</sup> Solar System Exploration Research Virtual Institute, NASA Ames Research Center, Mountain View, CA, USA

Received 2021 March 5; revised 2021 April 23; accepted 2021 April 29; published 2021 June 21

## Abstract

Permanently shadowed regions (PSRs) inside lunar polar craters likely harbor volatiles which are of great interest for both science and resource utilization. The origin and evolution of this resource is in part driven by external space weathering, including the bombardment by space plasma ions. Previous work has investigated the flux of horizontal solar wind ions that are deflected into lunar polar craters by plasma wake electrostatic fields. Here, we constrain the flux of ions that travel northward or southward in the natural environment encountered by the Moon along its orbit. Using 9 years of in situ ion measurements gathered by the ARTEMIS mission, we find that all locations inside lunar craters are altered by a flux of out-of-ecliptic ions of  $10^{-3}$  times the solar wind flux. In particular, the central floor of Shackleton's crater is weathered by a non-null ion flux. The origin of northward and southward ions impacting the Moon is identified as (i) shocked thermalized solar wind ions in the terrestrial magnetosheath and (ii) the isotropic component of ion distributions in the terrestrial magnetotail. The energy spectrum of out-of-ecliptic ions is found to be flatter than the solar wind spectrum. Thus, sputtering of pure water ice irradiated by out-of-ecliptic ions would be created for more than 30% by  $>3$  keV protons, unlike equatorial locations that are mostly sputtered by 1 keV protons. Future work may investigate the influence of the low, but nonzero flux of out-of-ecliptic ions reported here on the budget of volatiles in lunar PSRs.

*Unified Astronomy Thesaurus concepts:* [The Moon \(1692\)](#); [Solar wind \(1534\)](#); [Planetary magnetospheres \(997\)](#)

## 1. Introduction

### 1.1. Weathering of Permanently Shadowed Regions Inside Lunar Polar Craters

The obliquity of the Moon is only  $6.7^\circ$ , so that craters located near the lunar poles may harbor Permanently Shadowed Regions (PSRs). The cold environments of PSRs may accumulate and retain volatiles and are therefore of great interest for science and resource utilization (e.g., Arnold 1979; Nozette et al. 2001; Prem et al. 2020). As the Moon does not have an atmosphere or present-day global magnetic field, lunar polar crater PSRs are altered by external processes such as micrometeoroid bombardment, large impactors and possibly by space plasma electrons and ions. The role of impactors and space plasma particles on the volatile budget in PSRs is ambivalent: they act as both a source of elementary bricks required to create volatiles (including hydroxyl and water) (e.g., Füri et al. 2012), but they also vaporize, sputter, displace, and bury volatiles (e.g., Farrell et al. 2013, 2015; Szalay et al. 2019). A first step toward understanding the origin and evolution of volatiles in PSRs is the characterization of the influx of micrometeoroids and space plasma particles at each location inside lunar polar craters. Crater walls do not seem to protect PSRs from interplanetary dust, as their flux inside lunar craters may be as strong as anywhere else on the lunar surface, mostly because of the north and south toroidal source of dust originating from long-period comets (Pokorný et al. 2020). In this article, we further constrain the flux of space plasma ions weathering the interiors of lunar polar craters.

### 1.2. Space Plasma Ions which Bombard Lunar Polar Crater Interiors

To zeroth order, the majority of space plasma ions impacting the Moon originate in the solar wind, which consists of a beam of  $\sim 1$  keV/nucleon ions flowing parallel to the ecliptic plane, and therefore does not weather lunar polar crater interiors at all. However, we introduce hereafter the three known mechanisms by which ions access inside lunar polar craters: (1) the horizontal solar wind ion beam can be locally deflected into craters by ambipolar electric fields; (2) there are, in the natural environment encountered by the Moon along its orbit, ions traveling out of the ecliptic plane, northward or southward, which therefore directly enter into lunar polar craters; and (3) there are ions coming from the Moon itself.

(1) Plasma wakes are created inside lunar polar craters as the solar wind flows horizontally over them. The subsequent refilling of plasma wakes by electrons leads to the generation of ambipolar electric fields that deflect horizontal ions inside polar craters (Farrell et al. 2010, 2019; Zimmerman et al. 2011, 2012, 2013; Rhodes & Farrell 2020). Rhodes & Farrell (2020) have computed the flux of solar wind ions that impact this way at all locations inside four craters near the lunar South Pole: Shackleton, Haworth, Shoemaker, and Faustini. The previous authors found that the flux of deflected solar wind ions impacting most locations inside these craters is on the order of  $10^{-3}$  to  $10^{-1}$  times the horizontal solar wind flux. The topography inside craters appears to shield pocket valleys against deflected ions, where their flux may be zero. In addition, the width-to-depth ratio of Shackleton makes it different from the three other craters, as Rhodes & Farrell (2020) point out that the flux of electrostatically deflected ions is zero in a large region of Shackleton's central floor.



Original content from this work may be used under the terms of the [Creative Commons Attribution 4.0 licence](#). Any further distribution of this work must maintain attribution to the author(s) and the title of the work, journal citation and DOI.

(2) In the solar wind, the ion bulk velocity can be deflected out of the ecliptic plane during transient events. For instance, Gosling et al. (1997) reported north and south ion flow deflections of more than  $8^\circ$  above and below the ecliptic plane during the passage of a Corotating Interaction Region. In addition, the natural environment of the Moon comprises ion populations not encountered by asteroids simply bathed in the solar wind, because of the presence of the terrestrial magnetosphere. When the Moon is upstream of the Earth bow shock, it is bombarded by energetic foreshock ions (with kinetic energies typically  $>1$  keV) traveling away from the bow shock (Eastwood et al. 2005; Nishino et al. 2017; Xu et al. 2018). In the magnetosheath region, shocked thermalized solar wind ions may be deflected enough to access lunar polar crater interiors.

Finally, ions traveling northward or southward may exist in the terrestrial magnetotail which is crossed by the Moon for  $\sim 5$  days per lunar orbit. Three dynamic plasma environments are encountered by Earth's satellite in the geomagnetic tail, namely the plasma sheet, the plasma sheet boundary layer and the tenuous lobes. Positively charged particles there may consist of both solar wind ions ( $H^+$ ,  $He^{++}$ ) and terrestrial ionospheric ions ( $H^+$ ,  $He^+$ ,  $O^+$ ,  $N_2^+$ ,  $NO^+$ ,  $O_2^+$ ) (e.g., Poppe et al. 2016; Terada et al. 2017).

(3) The Moon and its exosphere affect the local ion environment and generate ion populations referred as “lunar ions” hereafter. The region of influence of the Earth's satellite on plasma ion distributions is sometimes called the “ion forenoon” region (e.g., Harada & Halekas 2016). Ion populations in the ion forenoon region include: (1) solar wind ions backscattered from the lunar surface (e.g., Saito et al. 2008; Lue et al. 2018), (2) solar wind ions reflected from magnetic anomalies (e.g., Nishino et al. 2009; Lue et al. 2011; Xu et al. 2020), (3) heavy ions sputtered from the lunar surface (e.g., Halekas et al. 2012), and (4) exospheric pickup ions (e.g., Yokota et al. 2009; Poppe et al. 2013b). In addition, 15% to 20% of solar wind protons are backscattered from the lunar surface as hydrogen Energetic Neutral Atoms (ENAs; e.g., Wieser et al. 2009; Vorburger et al. 2013). Reionized ENAs then possibly form another pickup ion population (never detected to date) that might weather lunar polar crater interiors.

The flux of “lunar” ions that impact the interiors of lunar polar craters is unknown, but we note that backscattered and reflected solar wind ions may have gyroradii smaller than the lunar radius (Harada & Halekas 2016), so that they may enter inside lunar polar craters. Heavy ions sputtered from the lunar surface have such large gyroradii that they may not re-impact the Moon. Exospheric ions can be created anywhere around the Moon, so that an unknown fraction of them should directly weather lunar PSRs.

Previously, Poppe et al. (2018) compiled omnidirectional (averaged over all look directions) ion observations collected from 2012 to 2018 by the Acceleration, Reconnection, Turbulence, and Electrodynamics of the Moon's Interaction with the Sun (ARTEMIS) mission. They determined the long-term averaged omnidirectional flux of ions in the natural environment encountered by the Moon as a function of ion kinetic energy and position of the Moon around Earth (i.e., upstream of the bow shock, in the terrestrial magnetosheath and in the magnetotail). Here, we constrain northward and southward ion fluxes that directly enter inside lunar polar craters (population 2 above) by analyzing directionally resolved ion flux observations gathered by ARTEMIS from 2012 to 2021.

The analyzed data set and the methods used to process it are introduced in Section 2. Section 3 then presents the characteristics of the long-term flux of out-of-ecliptic ions, which are compared with the flux of electrostatically deflected ions computed by Rhodes & Farrell (2020) (population 1 above). Our findings are summarized and discussed in Section 4, where future areas of research are also highlighted. In particular, the contribution of lunar ions to “self-weathering” effects in lunar polar crater interiors deserves future investigation (population 3 above).

## 2. Using the ARTEMIS ESA Data Set to Determine the Flux of Out-of-ecliptic Ions Weathering Lunar Polar Crater PSRs

### 2.1. The two ARTEMIS Probes in the $X_{SSE} > 3 R_L$ Region

This study relies on in situ ion measurements collected by the two probes of the ARTEMIS mission (Angelopoulos 2010). As highlighted by Poppe et al. (2018), the ARTEMIS ion data set is the best to date to estimate the long-term averaged ion environment seen by the Moon, thanks to the mission's 9 yr longevity, ion instruments put on board the satellites and the fact that the probes, in orbit around the Moon, co-orbit around Earth with the natural satellite in the different plasma regions it encounters: upstream of the bow shock, in the terrestrial magnetosheath and in the magnetotail. The two ARTEMIS probes, named ARTEMIS P1 and P2, are in highly elliptical near-equatorial orbits with periselene altitudes varying between 10 and  $\sim 1000$  km and apselenes located between 10 and 12  $R_L$  from the center of the Moon ( $R_L$  is the lunar radius,  $1 R_L = 1737$  km).

As introduced in Section 1.2, observations in the “ion forenoon” region may contain lunar ions. However, the traveling direction of a lunar ion observed locally by an ARTEMIS probe does not necessarily determine whether this ion subsequently impacts lunar polar crater interiors. For instance, a reflected proton observed close to the equator by an ARTEMIS probe and seen traveling northward could be misinterpreted as having access to South Pole craters, whereas it may in fact not impact the Moon at all.

Thus, to exclude this potential “contamination” from the study of northward and southward ion streams encountered in the natural environment crossed by the Moon, we only use measurements collected far upstream of the Moon, at  $X_{SSE} > 3 R_L$  (SSE is the Selenocentric Solar Ecliptic system). When the Moon is upstream of the terrestrial bow shock, the solar wind convects lunar ions downstream of the Moon. This is confirmed by the statistical study of lunar ions by Harada et al. (2015) which shows that the data selection criterion that we use,  $X_{SSE} > 3 R_L$ , ensures that we do not capture lunar ions when upstream of the terrestrial bow shock. In addition, all lunar ion detections reported when the Moon is in the magnetosheath or magnetotail regions happened at distances to the lunar center lower than  $2 R_L$  (e.g., Tanaka et al. 2009; Poppe et al. 2012; Halekas et al. 2015; Cao et al. 2020). Lunar ions generated in the tail lobes, where the convection velocity is reduced compared with the solar wind, may access the  $X_{SSE} > 3 R_L$  equatorial region that we study here. However, this happens for very specific and unlikely convection velocity and magnetic field configurations (Poppe et al. 2013a).

We average data collected from January 2012 to January 2021. The ARTEMIS P1 and P2 probes spent during this time

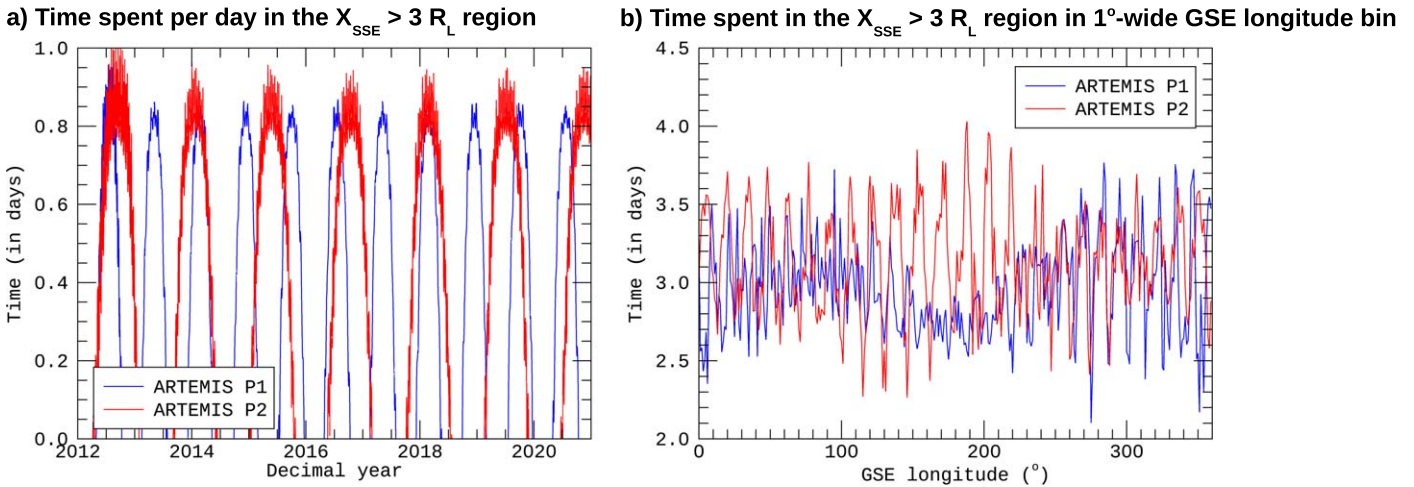


**Figure 1.** Panel (a): time spent by each of the two ARTEMIS probes in the  $X_{SSE} > 3 R_L$  region per day, from 2012 to 2021 January. Panel (b): Total time spent by each probe in the  $X_{SSE} > 3 R_L$  region in  $1^\circ$  wide GSE longitude bins, which represent different positions of the Moon around Earth.

period a total time of respectively 1065 days and 1129 days in the studied  $X_{SSE} > 3 R_L$  region. Figure 1(a) shows the time spent by each ARTEMIS probe in the  $X_{SSE} > 3 R_L$  region each day of the 2012–2021 period. It can be seen that the rotation of the Earth-Moon system around the Sun repeatedly brought the ARTEMIS probe line-of-apsides close to the Sun-Earth direction, when the spacecraft can sample the  $X_{SSE} > 3 R_L$  region. It can also be seen that the ARTEMIS probes’ orbital period of around 26 hours make them spend, on some days, entire days in the  $X_{SSE} > 3 R_L$  region. The data set used here frequently sampled the conditions seen by the Moon from 2012 to 2021, and using data from the two probes together further improves the time coverage (Figure 1(a)). We can therefore average together these measurements to construct a long-term averaged picture of the ion environment seen by the Moon, as done at Phobos around Mars by Nénon et al. (2019, 2021). Figure 1(b) shows the time spent by each of the two ARTEMIS probes in the region of interest in  $1^\circ$ -wide GSE longitude bins, i.e., as a function of the position of the Moon around Earth (GSE is the Geocentric Solar Ecliptic system). The total observing times of 1065 days and 1129 days for ARTEMIS P1 and P2 are distributed so that each probe spent a total of 2.5–3.5 days in each  $1^\circ$  GSE longitude bin.

## 2.2. Averaging Ion Observations Collected from 2012 to 2021 by the ARTEMIS ESA Experiment

The ARTEMIS probes each carry two experiments designed to observe space plasma ions: the ElectroStatic Analyzer (ESA; McFadden et al. 2008a, 2008b) which observes ions with kinetic energy per charge lower than 30 keV/q, and the Solid State Telescope (SST) experiment which observes 30 keV to several MeV ions. The angular resolution of SST data products is too coarse to constrain northward and southward ion fluxes, so that we only report on observations by ARTEMIS ESA.

ESA anodes observe  $180^\circ$  in a plane that contains the spin axis of the satellites, so that a  $4\pi$  steradian coverage is achieved each 3.25 s satellite spin period. Ion data are collected according to different modes and packed into various data products with different resolutions in time, kinetic energy per charge and solid angle. We use here the “Full” data product collected in the two modes “Magnetospheric Fast Survey” and “Magnetospheric Slow Survey.” In these data products, ion

observations are organized in 32 energy bins and 88 angular sectors. Each observation is a 1-spin 4 s snapshot obtained either every 32 spacecraft spins (“Fast Survey” mode) or 128 spacecraft spins (“Slow Survey” mode). We find that we average together 539,559 independent data points (each consisting of a 32 energy bins by 88 angular sectors table) collected in the  $X_{SSE} > 3 R_L$  region by the two ARTEMIS probes from January 2012 to January 2021.

The ARTEMIS P1 and P2 data sets are combined and we average the two-probe data set in  $1^\circ$  wide GSE longitude bins that represent the position of the Moon around Earth. Background ion counts are created by particles penetrating the instrument housing and by natural radioactivity in the ESA microchannel plate detectors (McFadden et al. 2008a, 2008b; Halekas et al. 2014). Background count rates were estimated and removed from observed count rates before conversion to ion flux in each GSE longitude bin independently. To compute the background, we have averaged, in each GSE longitude bin, count rates observed over the entire time period by the lowest energy bin of the instrument (i.e., the one most likely to show only background counts). This method accounts for time variation of the background linked to solar wind events, to the long-term variability of galactic cosmic ray particle fluxes and to possible energetic electrons in the terrestrial current sheet. Finally, recorded ion kinetic energies are corrected for the spacecraft surface potential, as measured by the Electric Field Instrument (EFI; Bonnell et al. 2009).

The 88 angular bins of the ESA data products analyzed here are defined in the ARTEMIS Despun, Sun-pointing,  $L$ -vector (DSL) coordinate system.  $Z_{DSL}$  is aligned with the spin axis of the spacecraft, the  $X_{DSL}$ - $Z_{DSL}$  plane contains the Sun direction (with X positive toward the Sun) and Y completes the orthogonal system (Angelopoulos 2009). From 2012 to 2021,  $Z_{DSL}$  made an angle with  $Z_{GSE}$  between  $164^\circ$  and  $172^\circ$  for the two ARTEMIS probes. Ions traveling anti-sunward along  $-X_{GSE}$  are therefore observed with a traveling DSL longitude, noted  $\varphi_{DSL}$ , that changed only very slightly over time between  $179^\circ.8$  and  $180^\circ.2$  and DSL latitudes, noted  $\theta_{DSL}$ , varying between  $-15^\circ$  and  $+12^\circ$ . We present in Section 3 anisotropy maps of ion fluxes in DSL coordinates to not distort angular sectors by converting them to another coordinate frame. In addition, working with the DSL coordinate system eases the integration of ion fluxes over look directions, as in particular

the orientation of DSL with respect to GSE changes over time. However, the  $8^{\circ}$ – $16^{\circ}$  angular offset between the DSL and GSE coordinate systems needs to be properly considered when interpreting ion fluxes integrated over look directions in the DSL system (see Section 3.2).

We finally note that the ARTEMIS ESA experiment cannot identify either the charge or mass of observed ions. We can therefore report hereafter only on ion kinetic energy per charge, and not ion kinetic energy, and cannot use ion mass or mass per charge information to further identify the origin of observed ions (e.g.,  $\text{He}^{++}$  of the solar wind or  $\text{O}^{+}$  ions from the terrestrial ionosphere).

### 3. Long-term Averaged Fluxes of Ions Impacting the Moon on its Subsolar and Antisub-solar Points, and Inside Polar Craters

#### 3.1. Long-term Averaged Anisotropy of Ion Fluxes

Figure 2 gives for selected positions of the Moon around Earth (GSE longitude) the long-term averaged flux of 700 eV/q and 9000 eV/q ions as a function of ion traveling direction in DSL coordinates (see Section 2.2). Upstream of the terrestrial bow shock in either the dawn sector (Figure 2(a)) or dusk sector (Figure 2(g)), 700 eV/q solar wind ions mostly travel anti-sunward. Suspicious high latitude fluxes are seen in the  $\varphi_{\text{DSL}} = 180^{\circ}$ – $225^{\circ}$  angular sectors. This appears to be an instrument artifact that has not been removed by the background correction method (see Section 2.2). We later show in Section 3.2 that it does not impact the conclusions of this study. At 9 keV/q, two ion populations are observed upstream of the bow shock (Figures 2(b), (h)): (1) energetic ions traveling anti-sunward and (2) terrestrial foreshock ions that travel away from Earth, likely along magnetic field lines connecting the spacecraft to the bow shock (noting, for instance, that a  $\varphi_{\text{DSL}}$  of  $270^{\circ}$  corresponds to a GSE direction longitude near  $90^{\circ}$ ). The high-latitude noise reported at 700 eV/q is not seen at 9 keV/q (Figures 2(b), (h)). We note that foreshock ion signatures seem broader in panel (h) than in panel (b). However, this may be linked to instrument background rather than to characteristics of these ions. Indeed, averaged foreshock ion fluxes are lower in panel (b) than in panel (h), so ion fluxes in angular sectors surrounding the peak sector in panel (b) may be below the instrument background level.

In the magnetosheath region downstream of the Earth bow shock (Figures 2(c)–(d)), some shocked heated ions are seen to travel away from Earth, while others have been deflected enough to reach elevation angles larger than  $45^{\circ}$  in absolute value. As we show in later sections, these high-elevation ions may directly enter inside lunar polar craters.

Deep in the terrestrial magnetotail (Figures 2(e)–(f)), both 700 eV/q and 9000 eV/q ions show an isotropic component that leads to the existence of ions traveling northward and southward, which can therefore directly enter South Pole and North Pole craters, respectively. Isotropic distributions in the magnetotail for 100 s of eV to 10 s of keV ions were already reported at distances of 20 Earth radii ( $R_{\oplus}$ ) from the center of Earth by Walsh et al. (2011) using Cluster observations and Wang et al. (2013) using THEMIS observations. The physical processes that act to isotropize ion distributions in the tail are not fully understood or conclusively identified (Walsh et al. 2011). We report here that similar isotropic distributions are observed at lunar distances of  $\sim 60$  Re downtail. For 9000 eV/q

ions, an additional population of earthward and tailward ions is observed (Figure 2(f)), likely because of reconnection events at the near X-line (generating tailward ions at the Moon) and distant X-line (earthward ions). One can see that the Moon is exposed to as much earthward energetic ion flux as tailward ion flux, as already reported by Kiehas et al. (2018) based on ARTEMIS ESA ion measurements.

#### 3.2. Origin of Ion Fluxes Impacting the Subsolar, Antisub-solar, and Polar Points on the Moon

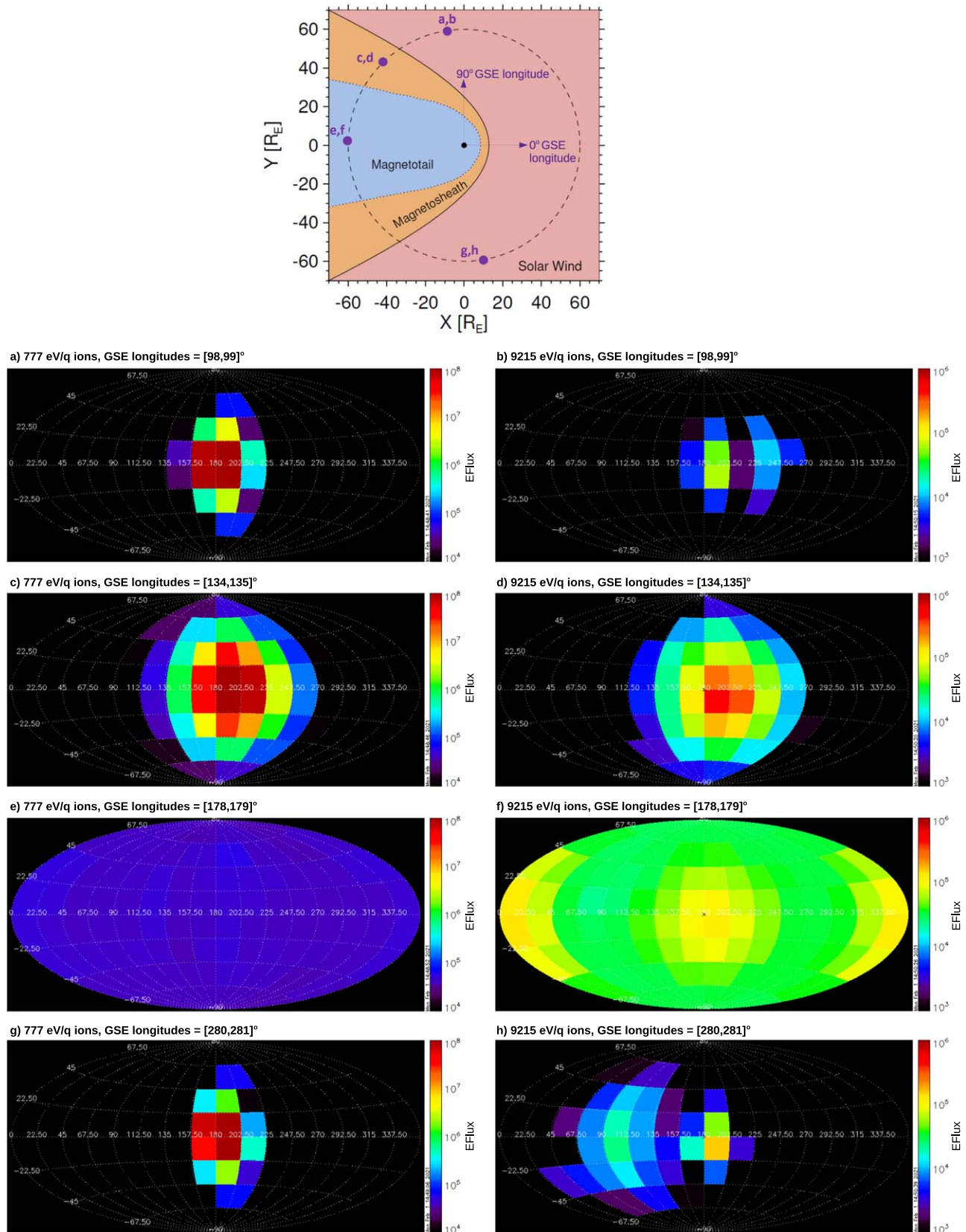
Ion fluxes determined from the ARTEMIS observations are then integrated over appropriate angular sectors to compute the flux of ions that impact the Moon at four points: (1) subsolar point, (2) antisub-solar point, and the flux of ions directly weathering the interior of lunar craters located near (3), the North Pole, and (4) the South Pole. At each of these four points on the Moon, we performed two integrations over look directions in DSL coordinates (Section 2.2). The first integration is obtained by taking into account all ions coming from within a cone around the local zenith with a half-opening angle of  $45^{\circ}$ . The second integration is performed within a cone with a half-opening angle of  $22.5^{\circ}$ . The choice of these two opening angles is driven by the  $22.5^{\circ}$  elevation width of the ESA angular sectors. Using a cone with a half-opening angle of  $45^{\circ}$ , we can compute the flux of ions that directly weather the center of Shackleton crater. Indeed, this point is exposed to all ion velocities making an angle with the local normal lower than  $57^{\circ}$  (see Figure 1 of Rhodes & Farrell 2020), and averaging ion observations over  $45^{\circ}$  in DSL coordinates may show ions coming from a direction inclined with the local normal of at maximum  $60^{\circ}$  (see Section 2.2). Using an integration cone with a half-opening angle of  $22.5^{\circ}$  enables to extract the most vertical ions.

Figure 3 shows the long-term averaged flux of ions that impact the subsolar, antisub-solar, and polar points as a function of GSE longitude of the Moon around Earth and ion kinetic energy per charge. Boundaries between the region upstream of the bow shock, the magnetosheath, and the magnetotail are identified with red vertical dashed lines, based on the results of Poppe et al. (2018). As expected, ions impacting the subsolar point have a lower flux and a broader kinetic energy range when the Moon crosses the magnetotail (Figures 3(a), (b)).

When the Moon is upstream of the terrestrial bow shock in the undisturbed solar wind, the flux of ions reaching lunar polar crater interiors (Figures 3(e)–(h)) is mostly below the ARTEMIS ESA background level. One can see at kinetic energies from 300 eV/q to 2000 eV/q the high latitude noise identified in Section 3.1, that is likely an instrument artifact. A real signal of out-of-ecliptic ions impacting lunar polar crater interiors is found at GSE longitudes between  $240^{\circ}$  and  $280^{\circ}$  with kinetic energies as high as 10 s of keV. The location and kinetic energies of these ions make them likely to be terrestrial foreshock ions. Foreshock ions may slightly access the antisub-solar point of the Moon (Figures 3(c)–(d)).

In the terrestrial magnetosheath, some shocked ions are thermalized enough to access lunar polar crater interiors (Figures 3(e)–(h)) but cannot access the antisub-solar point (Figures 3(c)–(d)). Finally, most of the ion flux impacting the polar and antisub-solar points is encountered when the Moon is in the magnetotail region, where ion fluxes are quasi-isotropic.

Figures 4(a) and (b) give the ion flux impacting respectively the subsolar point and polar points, averaged within a  $45^{\circ}$



**Figure 2.** Top panel: positions of the Moon around Earth for which 3D ion distributions are shown in panels (a)–(h). Panels (a)–(h): Long-term averaged flux of 700 eV/q and 9000 eV/q ions observed by ARTEMIS ESA in selected GSE longitude bins (position of the Moon around Earth, see top panel). Direction-resolved fluxes are shown as a function of ion traveling direction in the DSL coordinate frame (see Section 2.2). Ions traveling with a longitude of  $180^\circ$  (middle of the panels) travel away from the Sun. Ions traveling toward  $+90^\circ$  North in the shown DSL coordinate system travel toward the ecliptic South. EFlux is the ion energy flux in eV/(eV cm<sup>2</sup> s sr), computed by multiplying the ion differential flux with the ion kinetic energy.

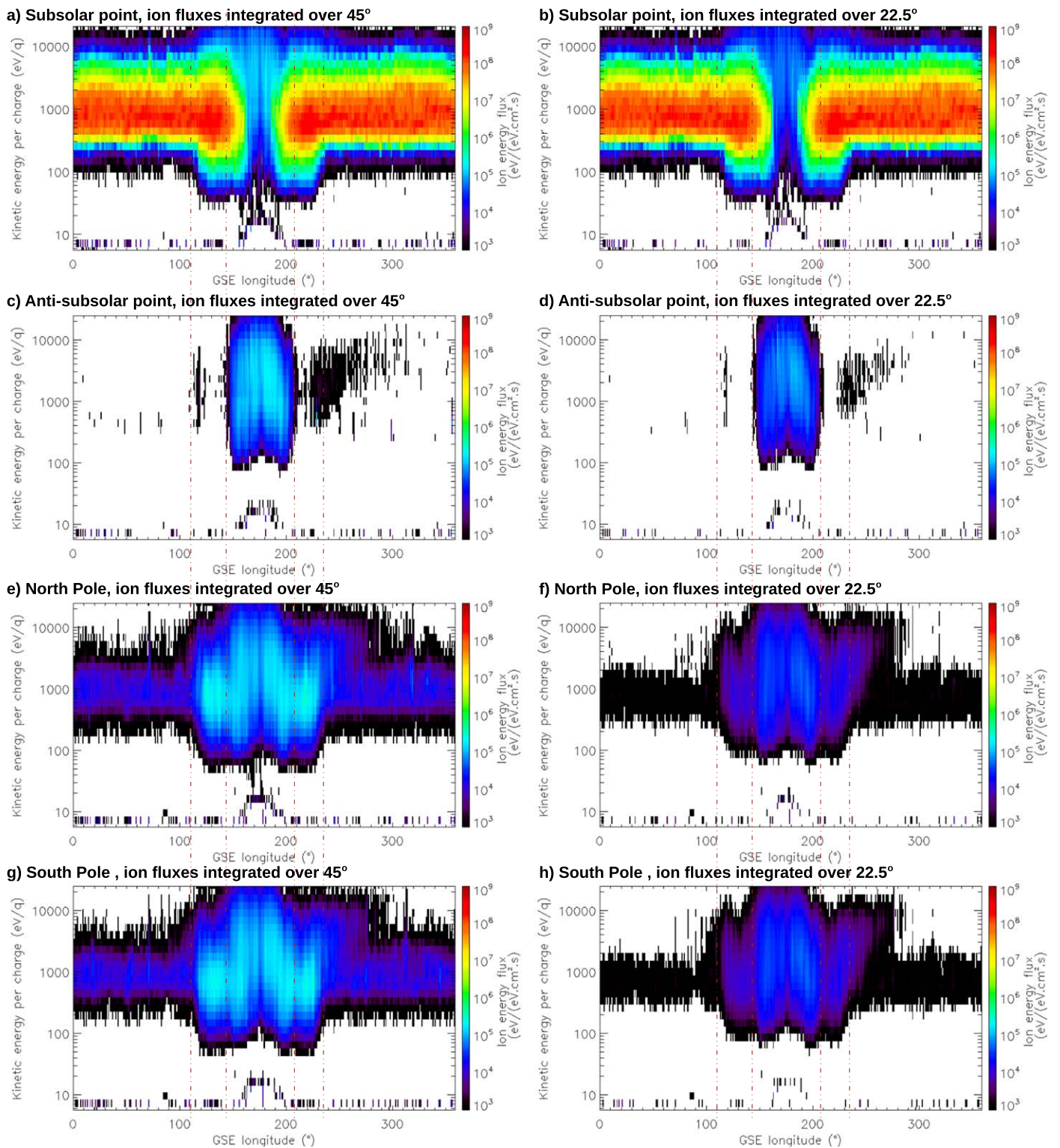
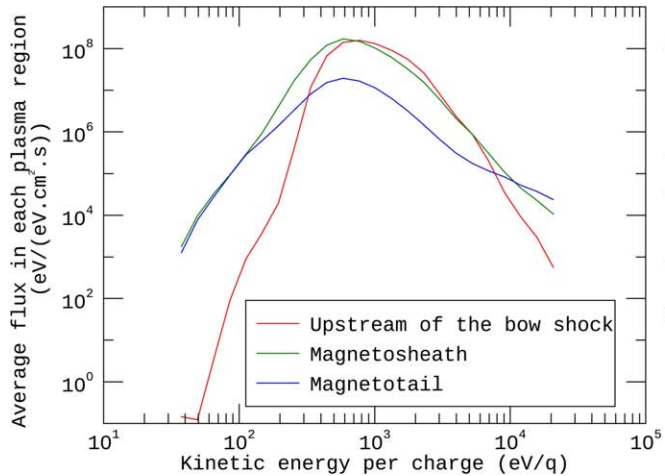


**Figure 3.** Long-term averaged ion flux impacting four points on the Moon as a function of the natural satellite position around Earth (GSE longitude) and ion kinetic energy per charge. Direction-resolved ion fluxes are integrated over look directions, by considering a cone around the local zenith with half-opening angle of  $45^\circ$  (panels (a), (c), (e), (g)) or  $22.5^\circ$  (panels (b), (d), (f), (h)).

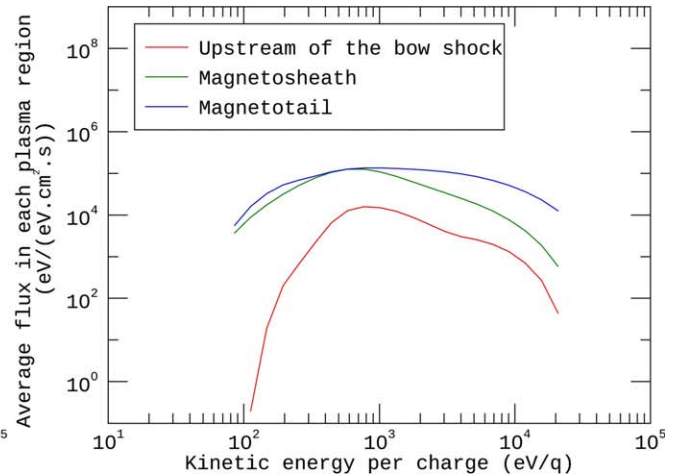
direction cone, in each plasma region encountered by the Moon (upstream of the bow shock, magnetosheath, magnetotail). Figures 4(c) and (d) give the ion fluence, computed by multiplying the ion flux by the time spent by the Moon in each region, then divided by a lunation period. This way, the black curves on Figures 4(c) and (d) give the lunation-averaged flux.

Figures 4(c) and (d) enable us to identify how much of the lunation-averaged ion flux comes from each plasma region. Ion fluxes impacting crater interiors near the North Pole and South Pole are found to be the same (Figures 3(e)–(h)), so that only South Pole fluxes are shown on Figures 4(b) and (d). Ions that impact the subsolar point at high ( $>10^4$  eV/q) and low

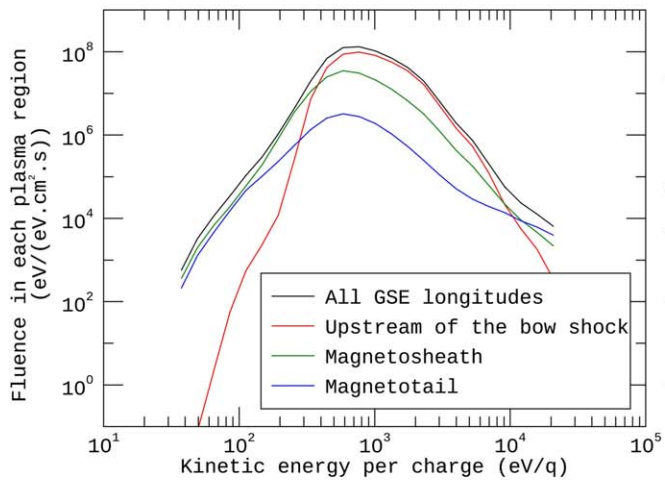
**a) Ion flux on subsolar point**



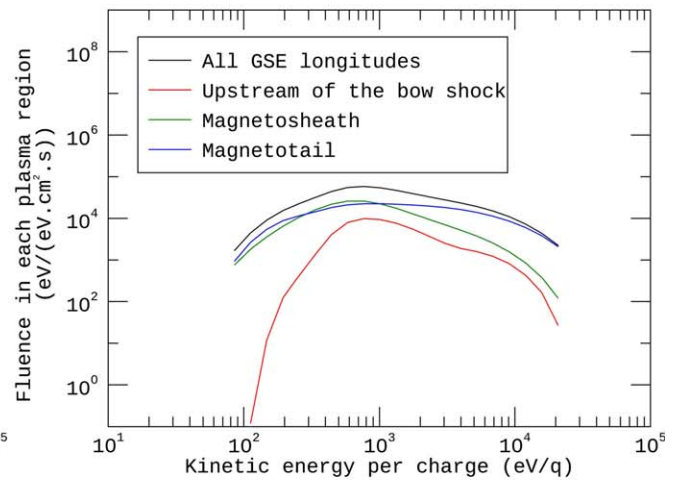
**b) Ion flux inside lunar polar craters**



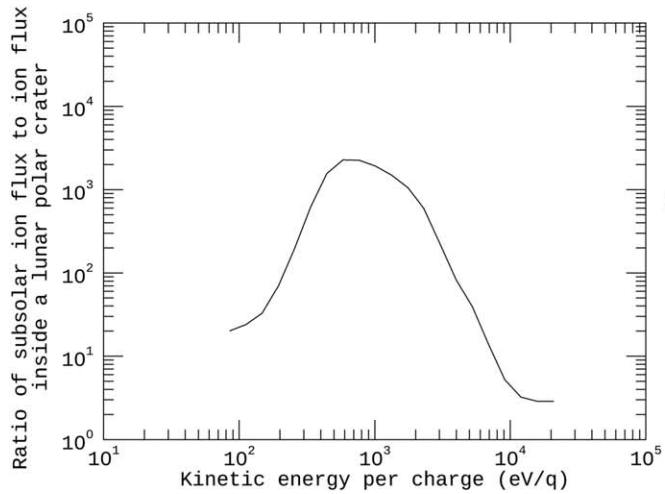
**c) Fluence on subsolar point**



**d) Fluence inside lunar polar craters**



**e) Ratio of subsolar to polar ion flux, averaged over all GSE longitudes**



**f) Ion flux on anti-subsolar point**

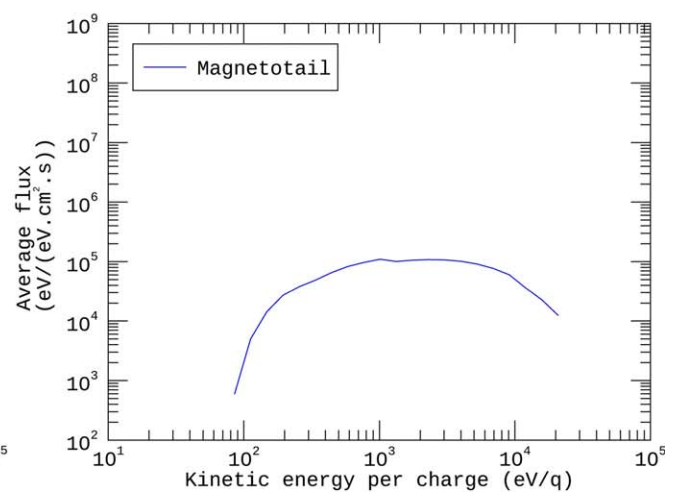


**Figure 4.** Panel (a): averaged ion flux impacting the subsolar point, encountered in the three plasma regions crossed by the Moon, averaged over look directions within a  $45^\circ$  integration cone. Panel (b): same as panel (a) for ions entering craters located near the South Pole. Panel (c): contribution of ion fluences encountered in the three plasma regions crossed by the Moon to the lunation-averaged flux of ions impacting the subsolar point, averaged over look directions within a  $45^\circ$  integration cone. Panel (d): same for ion fluences entering craters located near the lunar South Pole. Panel (e): ratio at each kinetic energy per charge of lunation-averaged ion fluxes (panels (c)–(d)) impacting the subsolar point and entering inside polar craters.

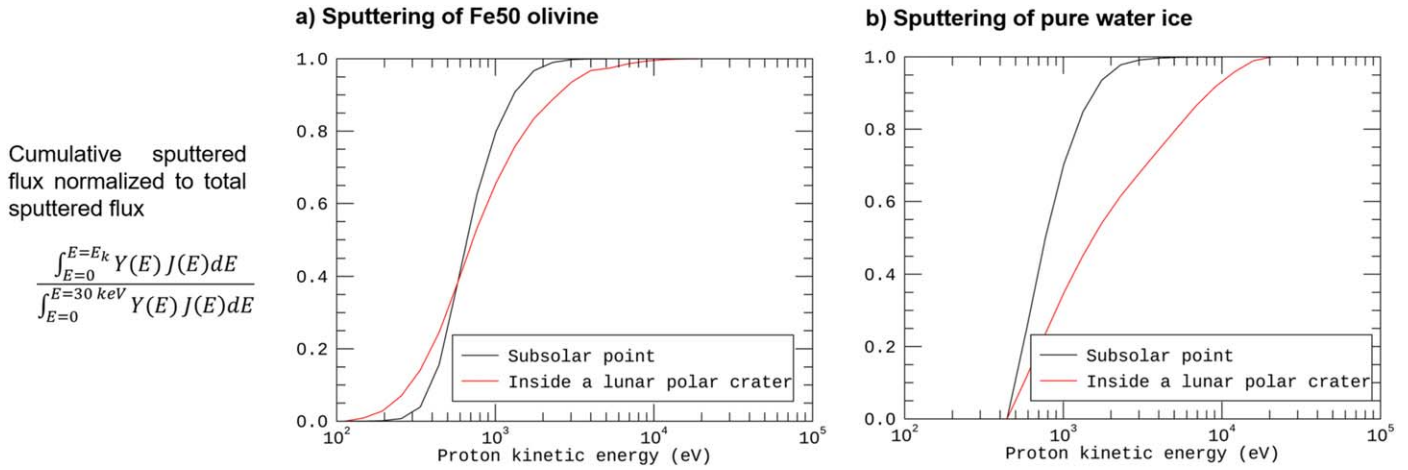


**Figure 5.** Flux of neutral particles sputtered from a surface by protons with kinetic energies between 0 and the abscissa kinetic energy, normalized by the flux sputtered by all proton kinetic energies together. Panel (a): for Fe50 olivine with a density of 3.8 g/cc using sputtering yields from Nénon & Poppe (2020). Panel (b): for pure water ice, using sputtering yields from Cassidy et al. (2013).

(<400 eV/q) kinetic energies (Figure 4(c)) are mostly encountered when the Moon is in the magnetosheath and magnetotail regions.

The fluence of out-of-ecliptic ions entering lunar polar craters while the Moon is upstream of the bow shock (red curve on Figure 4(d)) is negligible compared with fluences in the magnetosheath and magnetotail regions (green and blue curves on Figure 4(d)). We therefore find that the noise reported in Section 2.2, which is clearly visible as the  $\sim 700$  eV/q bump (red curve), does not impact the conclusions of our study, as its contribution is negligible over magnetosheath and magnetotail ion fluences. Above a few keV/q, ions that directly weather polar crater interiors mostly come from crossings of the Moon in the terrestrial magnetotail (blue curve on Figure 4(d)), even if the natural satellite only spends 5 days per lunar orbit there. For completeness, Figure 4(f) gives the flux of ions impacting the antisubolar point. As shown by Figures 3(c)–(d), these ions are almost exclusively encountered in the magnetotail.

### 3.3. Intensity of Out-of-ecliptic Ion Fluxes Entering Lunar Polar Craters

Figure 4(e) gives, as a function of ion kinetic energy per charge, the ratio of ion fluxes impacting the subsolar point to those directly entering lunar polar craters (averaged within an ion direction cone of  $45^\circ$ , see Section 3.2). At solar wind kinetic energies  $\sim 700$  eV/q, the lunation-averaged ion flux on the subsolar point is more than three orders of magnitude stronger than the flux of polar ions. However, the ratio of subsolar to polar ion fluxes is of only a factor of 3 at kinetic energies greater than 10 keV/q. This relatively low ratio comes from the isotropic component of 10 s of keV/q ions in the magnetotail (Figure 2(f)). The fact that ion fluxes on the subsolar point are a factor of 3 more intense than on polar regions at these kinetic energies comes from energetic tailward ions associated to reconnection events.

The flux of ions that directly enter lunar polar craters is, integrated over all ion kinetic energies, of  $1.7 \times 10^5 \text{ cm}^{-2} \text{ s}^{-1}$ , which is around one-thousandth of the solar wind flux ( $2 \times 10^8 \text{ cm}^{-2} \text{ s}^{-1}$ ). One can compare the flux of out-of-ecliptic ions computed here ( $10^{-3}$  the solar wind flux) with the flux of horizontal ions electrostatically deflected inside craters, shown on top crater maps by Figure 3 of Rhodes & Farrell (2020).

Some localized pocket valleys inside the craters Haworth, Shoemaker, and Faustini were found by the previous authors to be completely sheltered from deflected horizontal ions due to local topography. In addition, a large region around the central floor of Shackleton was proposed to be completely unaltered by space plasma ions (see Figure 3 of Rhodes & Farrell 2020). We find that these locations are in fact weathered by a flux of ions that is not zero but that is of at least  $10^{-3}$  times the solar wind flux. However, most locations inside the South Pole craters studied by Rhodes & Farrell (2020) are exposed to a flux of electrostatically deflected ions of  $10^{-2}$ – $10^{-1}$  the solar wind flux, where electrostatic deflection is therefore the dominant source of bombarding ion flux over out-of-ecliptic ions.

### 3.4. Out-of-ecliptic Ion Energy Spectrum and Surface Sputtering

As out-of-ecliptic ions are mostly encountered when the Moon crosses the terrestrial magnetosheath and magnetotail (Figure 3), their energy spectrum is flatter than the solar wind spectrum (Figure 4(d)). We study here the influence of ion energy spectra on sputtering of neutral particles from the surface, which is a fundamental process at airless bodies throughout the solar system. In particular, we investigate which ion kinetic energies contribute to sputtering due to ions impacting the subsolar point and polar regions, respectively. To do so, we have computed the flux of neutral atoms sputtered from a surface made of either Fe50 olivine ( $\text{MgFeSiO}_4$ ) or pure water ice. We note that water ice on the Moon is likely mixed with regolith (Li et al. 2018); however, we use pure water ice as an end-member test case. All observed ions are assumed to be protons and we use the energy-dependent sputtering yields published by Nénon & Poppe (2020) for Fe50 olivine with a density of 3.8 g/cc and those given by Cassidy et al. (2013) for pure water ice. Figures 5(a) and (b) give the cumulative distribution of neutral sputtered flux as a function of proton kinetic energy, i.e., the sputtered flux created by protons with kinetic energies going from  $E_k = 0$  to the abscissa kinetic energy, normalized by the neutral flux sputtered by all kinetic energies together. Sputtering of olivine and water ice at the lunar subsolar point is, as expected, generated by a narrow range of kinetic energies around 600 eV, as 80% (between 0.1 and 0.9 on the y-axis of Figure 5) of the total sputtered flux is

created by 400–1500 eV protons. Pure water ice exposed to only the flux of out-of-ecliptic ions would be sputtered a thousand times slower than at regions exposed to the solar wind. However, we reveal on Figure 5(b) that this process would be the result of the bombardment by ions with greater kinetic energies than the solar wind, as 50% of water ice sputtering would be due to  $>1.5$  keV protons and 20% due to  $>5$  keV protons (Figure 5(b)). This comes from the combination of (1) the relatively flat energy spectrum of out-of-ecliptic ions with (2) the energy dependence of the pure water ice sputtering yield, which increases with increasing proton kinetic energy.

#### 4. Summary and Discussion

Since 2012, the ElectroStatic Analyzer experiment (ESA) on board the two ARTEMIS probes has been collecting directionally resolved ion flux measurements in the environment encountered by the Moon along its orbit (upstream of the Earth bow shock, in the terrestrial magnetosheath and in the terrestrial magnetotail). This data set reveals the long-term averaged flux of ions which, in the natural environment that is not disturbed by the Moon itself, travel northward or southward and therefore directly enter lunar polar craters. The lunation-averaged flux of out-of-ecliptic ions is dominated by thermalized ions in the magnetosheath and by the isotropic component of ion distributions encountered in the terrestrial magnetotail (Figures 3 and 4).

As a result of the out-of-ecliptic ion population that bombards the Moon, we find that all locations inside lunar polar craters and PSRs are weathered by a long-term averaged flux of ions that is of at least  $10^{-3}$  times the solar wind flux. In particular, these ions bombard regions that are otherwise protected by topography from horizontal solar wind ions deflected by wake electric fields (Rhodes & Farrell 2020), including the central floor of Shackleton’s crater. The influence of out-of-ecliptic ions encountered in the terrestrial magnetosheath and tail on the life cycle and budget of volatiles on Shackleton’s central floor could be investigated in the future (e.g., Tucker et al. 2020) using the energy spectra reported on Figures 3 and 4.

The energy spectrum of out-of-ecliptic ions is broader than the solar wind spectrum. One consequence of this is that sputtering of pure water ice which would be irradiated only by out-of-ecliptic protons would be generated by protons more energetic than the typical 1 keV solar wind energy, as 50% of sputtering would be due to  $>1.5$  keV protons and 30% to  $>3$  keV protons.

Future work can be conducted along three lines of research to further identify the characteristics of ions that bombard and alter lunar PSRs. First, Rhodes & Farrell (2020) considered a perfectly horizontal ion beam while studying the deflection of ions inside lunar craters. Future efforts may consider the deflection of ions with non-null elevation angles. The coarse angular resolution of the ARTEMIS ESA data products does not enable a study of ion populations with low elevation angles, for instance ions traveling with an elevation angle of  $8^\circ$  above or below the ecliptic plane during the passage of a CIR (Gosling et al. 1997). However, observations of the solar wind with fine angular resolutions by the ACE and Wind spacecraft can be analyzed to study the influence of the distribution of solar wind elevation angles over time on the flux of electrostatically deflected ions inside lunar polar craters.

A second future line of work could investigate the flux of “lunar” ions impacting lunar polar crater interiors. In particular, solar wind protons reflected over magnetic anomalies have been reported to have densities as high as  $10^{-2}$  the solar wind density in the lunar wake (Xu et al. 2020). For conditions where these reflected protons had relatively smaller gyroradii (e.g., during periods of higher IMF strength), it may be possible that reflected protons gyrate directly into lunar polar regions as opposed to gyrating farther downstream and into the wake.

Finally, the specie of out-of-ecliptic ions that enter lunar polar craters is not measured by the ARTEMIS ESA ion experiment. Ion measurements with mass (or mass per charge) and directional resolution conducted in the terrestrial magnetotail at lunar distances would for instance enable us to constrain the flux of terrestrial  $O^+$  ions that may supply oxygen in lunar PSRs.

The authors gratefully acknowledge support from NASA’s Solar System Research Virtual Institute (SSRVI) via both the DREAM2 team, grant #NNX14AG16A, and the LEADER team, grant #80NSSC20M0060.

The ARTEMIS mission is funded and operated under NASA grant NAS5-02099, and we specifically acknowledge J. P. McFadden for the use of ESA data. All ARTEMIS data necessary to reproduce this work are publicly available at <http://artemis.ssl.berkeley.edu>.

#### ORCID iDs

Q. Nénon  <https://orcid.org/0000-0001-8130-9832>

A. R. Poppe  <https://orcid.org/0000-0001-8137-8176>

#### References

- Angelopoulos, V. 2009, in *The THEMIS Mission*, ed. J. L. Burch & V. Angelopoulos (New York: Springer), 5
- Angelopoulos, V. 2010, in *The ARTEMIS Mission*, ed. C. Russell & V. Angelopoulos (New York: Springer), 3
- Arnold, J. R. 1979, *JGR*, **84**, 5659
- Bonnell, J. W., Mozer, F. S., Delory, G. T., et al. 2009, in *The THEMIS Mission*, ed. J. L. Burch & V. Angelopoulos (New York: Springer), 303
- Cao, X., Halekas, J., Poppe, A., Chu, F., & Glassmeier, K. H. 2020, *JGRA*, **125**, e27829
- Cassidy, T. A., Paranicas, C. P., Shirley, J. H., et al. 2013, *P&SS*, **77**, 64
- Eastwood, J. P., Lucek, E. A., Mazelle, C., et al. 2005, *SSRv*, **118**, 41
- Farrell, W. M., Hurley, D. M., Hodges, R. R., et al. 2013, *P&SS*, **89**, 15
- Farrell, W. M., Hurley, D. M., Poston, M. J., et al. 2019, *GeoRL*, **46**, 8680
- Farrell, W. M., Hurley, D. M., & Zimmerman, M. I. 2015, *GeoRL*, **42**, 3160
- Farrell, W. M., Stubbs, T. J., Halekas, J. S., et al. 2010, *JGRE*, **115**, E03004
- Füri, E., Marty, B., & Assonov, S. S. 2012, *Icar*, **218**, 220
- Gosling, J. T., Bame, S. J., Feldman, W. C., et al. 1997, *GeoRL*, **24**, 309
- Halekas, J. S., Benna, M., Mahaffy, P. R., et al. 2015, *GeoRL*, **42**, 5162
- Halekas, J. S., Poppe, A. R., Delory, G. T., et al. 2012, *JGRE*, **117**, E06006
- Halekas, J. S., Poppe, A. R., & McFadden, J. P. 2014, *JGRA*, **119**, 5133
- Harada, Y., & Halekas, J. S. 2016, in *Low-Frequency Waves in Space Plasmas*, Vol. 216, ed. A. Keiling et al. (New York: Wiley), 307
- Harada, Y., Halekas, J. S., Poppe, A. R., et al. 2015, *JGRA*, **120**, 4907
- Kiehas, S. A., Runov, A., Angelopolos, V., Hietala, H., & Korovinskiy, D. 2018, *JGRA*, **123**, 1767
- Li, S., Lucey, P. G., Milliken, R. E., et al. 2018, *PNAS*, **115**, 8907
- Lue, C., Futana, Y., Barabash, S., et al. 2011, *GeoRL*, **38**, L03202
- Lue, C., Halekas, J. S., Poppe, A. R., & McFadden, J. P. 2018, *JGRA*, **123**, 5289
- McFadden, J. P., Carlson, C. W., Larson, D., et al. 2008a, *SSRv*, **141**, 277
- McFadden, J. P., Carlson, C. W., Larson, D., et al. 2008b, in *The THEMIS Mission*, ed. J. L. Burch & V. Angelopoulos (New York: Springer), 477
- Nénon, Q., & Poppe, A. R. 2020, *PSJ*, **1**, 69
- Nénon, Q., Poppe, A. R., Rahmati, A., et al. 2019, *JGRE*, **124**, 3385
- Nénon, Q., Poppe, A. R., Rahmati, A., & McFadden, J. P. 2021, *NatGe*, **14**, 61
- Nishino, M. N., Fujimoto, M., Maezawa, K., et al. 2009, *GeoRL*, **36**, L16103

- Nishino, M. N., Harada, Y., Saito, Y., et al. 2017, *Icar*, **293**, 45
- Nozette, S., Spudis, P. D., Robinson, M. S., et al. 2001, *JGR*, **106**, 23253
- Pokorný, P., Sarantos, M., Janches, D., & Mazarico, E. 2020, *ApJ*, **894**, 114
- Poppe, A. R., Farrell, W. M., & Halekas, J. S. 2018, *JGRE*, **123**, 37
- Poppe, A. R., Fillingim, M. O., Halekas, J. S., Raeder, J., & Angelopoulos, V. 2016, *GeoRL*, **43**, 6749
- Poppe, A. R., Halekas, J. S., Samad, R., Sarantos, M., & Delory, G. T. 2013a, *JGRE*, **118**, 1135
- Poppe, A. R., Halekas, J. S., Sarantos, M., & Delory, G. T. 2013b, *JGRE*, **118**, 1934
- Poppe, A. R., Samad, R., Halekas, J. S., et al. 2012, *GeoRL*, **39**, L15104
- Prem, P., Kereszturi, Á., Deutsch, A. N., et al. 2020, arXiv:2012.06317
- Rhodes, D. J., & Farrell, W. M. 2020, *PSJ*, **1**, 13
- Saito, Y., Yokota, S., Tanaka, T., et al. 2008, *GeoRL*, **35**, L24205
- Szalay, J. R., Pokorný, P., Sternovsky, Z., et al. 2019, *JGRE*, **124**, 143
- Tanaka, T., Saito, Y., Yokota, S., et al. 2009, *GeoRL*, **36**, L22106
- Terada, K., Yokota, S., Saito, Y., et al. 2017, *NatAs*, **1**, 0026
- Tucker, O. J., Farrell, W. M., & Poppe, A. R. 2020, *JGRE*, **126**, e06552
- Vorburger, A., Wurz, P., Barabash, S., et al. 2013, *JGRA*, **118**, 3937
- Walsh, A. P., Owen, C. J., Fazakerley, A. N., Forsyth, C., & Dandouras, I. 2011, *GeoRL*, **38**, L06103
- Wang, C. P., Zaharia, S. G., Lyons, L. R., & Angelopoulos, V. 2013, *JGRA*, **118**, 244
- Wieser, M., Barabash, S., Futaana, Y., et al. 2009, *P&SS*, **57**, 2132
- Xu, S., Poppe, A. R., Halekas, J. S., & Harada, Y. 2020, *JGRA*, **125**, e28154
- Xu, X., Chang, Q., Xu, Q., et al. 2018, *ApJ*, **863**, 80
- Yokota, S., Saito, Y., Asamura, K., et al. 2009, *GeoRL*, **36**, L11201
- Zimmerman, M. I., Farrell, W. M., & Stubbs, T. J. 2013, *Icar*, **226**, 992
- Zimmerman, M. I., Farrell, W. M., Stubbs, T. J., Halekas, J. S., & Jackson, T. L. 2011, *GeoRL*, **38**, L19202
- Zimmerman, M. I., Jackson, T. L., Farrell, W. M., & Stubbs, T. J. 2012, *JGRE*, **117**, E00K03